Transport of a sliding Wigner crystal in the four flux composite fermion regime

Chi Zhang,[1,2,*] Rui-Rui Du,[1,2] M. J. Manfra,[3] L. N. Pfeiffer,[4] and K. W. West[4]
[1]*International Center for Quantum Materials, Peking University, Beijing 100871, China*
[2]*Department of Physics and Astronomy, Rice University, Houston, Texas 77251, USA*
[3]*Department of Physics and Astronomy, Purdue University, West Lafayette, Indiana 47907, USA*
[4]*Department of Electrical Engineering, Princeton University, Princeton, New Jersey 08544, USA*
(Received 28 February 2015; published 24 August 2015)

In two-dimensional (2D) electron systems, Wigner crystals (WC) and fractional quantum Hall effect (FQHE) liquids are competing ground states under low temperatures (T) and high magnetic fields (B). Here we report differential conductivity results demonstrating the reentrant insulating phase around $\nu = 1/5$ in a 2D hole system in AlGaAs/GaAs quantum wells and unexpected features in the solid-liquid phase transition between WC and FQHE liquids in ultrahigh magnetic fields up to 45 T. Remarkably, the electric field (E) plays an equivalent role as the temperature does in our phase diagram. From the $E - T$ "duality" analysis, a characteristic length of 450 nm is derived, which can be understood as the phase-coherent domain size of WC. Moreover, evidence shows that with weak disorder the insulating phase and composite fermion liquid could be coexisting around $\nu = 1/5$, pointing to the possibility that the insulating phase is the four flux quantum Wigner crystal, as proposed by theories.

DOI: 10.1103/PhysRevB.92.075434 PACS number(s): 73.43.−f

I. INTRODUCTION

Wigner crystals (WC) [1] and fractional quantum Hall effect (FQHE) liquids [2] are the two types of electron matter that compete in the clean two-dimensional (2D) system under high magnetic fields. The physics concept of Wigner crystals was originally proposed in 1934 [1]: the electron liquid can be crystallized in a disorder free system, in which the Coulomb energy dominates the kinetic energy. The disorder potential can pin the WC, forming an insulating phase (IP). In dilute 2D systems, evidence for the WC was accumulated [3–6]: the Coulomb energy $E_C \propto n^{1/2}$, where n represents the carrier density, and the kinetic energy E_k is proportional to n. Conventionally, a dimensionless density r_s ($r_s \equiv E_C/E_k$) can be given in terms $r_s = (\pi n)^{-1/2}/a_B^*$, in which a_B^* denotes the effective Bohr radius. Due to the distinct effective mass difference between electron and hole GaAs systems, $a_B^* =$ 10.2 and 1.7 nm in 2-dimensional electron system (2DES) and 2-dimensional hole system (2DHS), respectively. As a result, a WC solid, which has been observed in Refs. [4,7–9], occurs for small r_s (∼1–3) for 2DES as compared to that of 2DHS ($r_s \sim 7$–15). Previous results reported the reentrant insulating phase (RIP) around $\nu = 1/5$ in 2DES [3,4,7] and $\nu = 1/3$ in 2DHS [5]. In more recent research on the phases of high magnetic field IP and reentrant IP in the 2DHS, r_s reaches a maximum around 37 by tuning the hole density [10,11].

Early theoretical proposals discussed the static and dynamical properties of WC based on the sinusoidal charge density wave [12] under magnetic fields [13]. The effect of disorder was discussed in two limits: first, the electrons locate at each impurity site in the strong pinning limit; second, in the weak pinning case with strong elastic energy the phase breaks into domains [14]. Subsequently, some recent theoretical works studied the role of the disorder with an elastic structure on vortices' lattices [15,16], in which some important characteristic length scales, i.e., the correlation length or domain size (denoted as the Larkin length [17,18]) of the crystalline order were identified. At the same time, some evidence of the pinning mode was obtained by a microwave experiment [19], in which a domain size of 100–200 nm was calculated.

Theoretically, at very low filling factors, the type-1 composite fermion Wigner crystal (CFWC) has lower energy than electron WC [20]. On the other hand, the weak disorder potential may also lead to the type-2 CFWC (or CF crystal) [21,22]. Archer and Jain's computations [21] are consistent with the experiments of Ref. [23]: the pinning mode for microwave resonance was observed in a range of $\nu \sim 1/3 \pm 0.015$, which is distinct to the wide range for electron crystals. In the range of $\nu \sim (2/9)$–$(1/5)$, there is the possibility of interplay between the type-1 and type-2 CFWC [22]. In the nearby fillings of fully occupied (CF) Λ levels (i.e., $\nu^* = 1$ for $\nu = 1/5$), the type-2 CF crystal may occur [21,22].

In this paper, we report the first observations of the reentrant insulating phase around the $\nu = 1/5$ FHQE state ($r_s \sim 7.6$) in 2DHS with a large effective mass in our wafer ($m^* = 0.4m_e$) [24]. The unique T-dependent magnetoconductivities display unexpected features: (1) at $\nu =$ 1/5, an insulating phase prevails at $T < 100$ mK, and "melts" into FQHE liquid for $T > 100$ mK; and (2) σ_{xx} shows a remarkable "Λ" shape as a function of $1/T$ in the flanks of $\nu = 1/5$ with a critical temperature $T_C \sim 200$ mK; i.e., σ_{xx} increases (and decreases) exponentially with $1/T$ above (and below) T_C, respectively. We interpret the "Λ" shape as the result of the robust FQHE liquid at 1/5 under intermediate temperature. The differential conductivity under the external electric field (E) in the IP regime shows a strong nonlinear response, indicating a pinned-to sliding-WC transition driven by an E field. Our results confirm that the Larkin length R_C of 450 nm is the domain size in the WC phase.

Remarkably, in 2DHS we observe the coexisting WC solid and CF liquid ($\nu = 1/5$ and 2/9), in the four flux CF regime, with $\nu = \frac{n}{2pn\pm1}$ and $2p = 4$ (integer $n = 1, 2$). In our study, weak disorder plays an important role, which leads to the

*gwlzhangchi@pku.edu.cn

domains in Wigner crystal and the possibility for the novel CF crystal. In this report, our motivations are (1) to obtain the domain size of the quantum solid and (2) to map out an empirical phase diagram in the regime of ^{4}CF.

II. EXPERIMENTAL RESULTS

Our experiments are performed in a dilution refrigerator, with a base temperature of 20 mK. In the National High Magnetic Field Laboratory at Tallahassee, Florida, the samples are studied in a $B \sim 45$-T hybrid magnet, which consists of the superconducting magnet (11.5 T) and a resistive magnet (33.5 T). This project is carried out in a carbon-doped GaAs/$Al_{0.24}Ga_{0.76}As$ narrow (20-nm-wide) quantum well (QW), with high hole density ($p = 2 \times 10^{11}$ cm^{-2}) and high mobility ($\mu = 1 \times 10^6$ cm^2/V s). In the measurements, our sample is patterned as a Corbino configuration [outer and inner diameters equal 2.5 and 1.25 mm, respectively; see inset, Fig. 1(a)], which has been widely used in conductivity measurements. The σ_{xx} measurements are conducted by applying a dc electric field (E_{dc}) which, for the simplest model of the Corbino sample, is along the radial direction, with the transverse component being eliminated. In Refs. [4,5], it is quite clear that the longitudinal resistance approaches zero, and the Hall resistivity is well quantized at FQHE, while extremely large R_{xx} and irregular Hall resistivity exist in the WC. Therefore, unlike the resistivity components R_{xx} and R_{xy} [4,5], σ_{xx} is the only component obtained in the Corbino measurements. The conductivity approaches zero in the FQHE liquid state (because of the tensor relation: $\sigma_{xx} \propto R_{xx}$ in 2D systems), and the measured "0" current reflects the WC insulating phase.

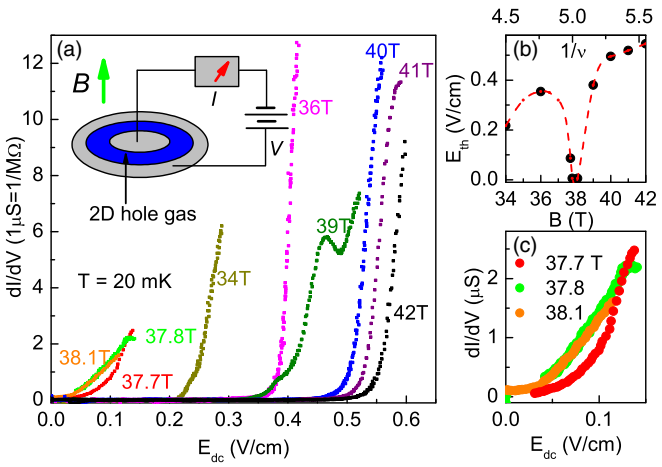

FIG. 1. (Color online) The results of the derivative conductivity (dI/dV) measurement. (a) For some magnetic fields (certain filling factors), the derivative conductivity shows the large threshold E field (E_{th}) and dramatic slope. $B = 34$- and 39-T data exhibit complex features, which come from the (2/9 and 1/5) FQHE liquid order in the mixing of WC-melted liquid. Inset: Schematic of the conductivity measurements on the Corbino sample. (b) The threshold for the electric field under magnetic fields and the corresponding $1/\nu$. (c) The linear or linearlike dI/dV features at $B = 37.7$, 37.8, and 38.1 T.

A. Nonlinear measurements

The noise measurements and the derivative conductance dI/dV in nonlinear experiments have been used to distinguish FQHE liquid and WC [7,9]. In fact, the block of WC can be pinned by the disorder potential in a real 2D system [25]. To overcome the disorder potential, the sliding motion of WC can be driven by a microwave or an external E field [19,26,27]. As referenced, Zhu *et al.* [27,28] predicted a practical method for probing the threshold E field to drive the sliding WC. Because both WC and FQHE show zero conductivity under magnetic fields, in this experiment we use dI/dV data to distinguish between the two. For fixed Landau-level filling factors (or B), the dI/dV measurements are conducted by sweeping the dc electric field from zero to high values. Our nonlinear results [Fig. 1(a)] exhibit the RIP around the filling factor $\nu = 1/5$: the dI/dV data display dramatic thresholds (E_{th}) for the B field ranging from 34 to 37 T and from 39 to 42 T. The thresholds under magnetic fields and $1/\nu$ are shown in Fig. 1(b); the red dashed line separates the solid and liquid phases. The trace of the linear derivative conductivity around $B \sim 38$ T [in Fig. 1(c)] is sharply distinct from that of the IP. The threshold almost diminishes at $B \sim 37.8$ and 38.1 T. The 37.7-T data show the transition between the liquid and solid phases, and show no clear threshold, with one slope existing for E exceeding 0.1 V/cm. In the WC regime, each dI/dV trace increases sharply, reaching a rather high value. At $B = 34$ T, the unusual trace shows a transitional behavior for the typical solids and liquid: (i) the threshold E_{th} is between "zero" (for the 1/5 FQH liquid) and 0.3–0.5 V/cm (for WC); (ii) the trace at 34 T can be separated into three sections: (a) the pinning section for $E < E_{th}$; (b) the narrow interval for the intermediate E-field regime displaying a small slope; and (c) the linear curve with a much larger slope, which is a typical behavior for the WC solid depinning. Section (b) is a narrow area that is considered as an insert in the process of WC depinning. In fact, section (b) of the trace at 34 T is consistent with the $\nu \sim 2/9$ FQHE liquid in the massive sliding WC. This complex behavior will be described and explained in the section of the phase diagram. Moreover, in the comparison between the $\nu = 1/5$ and 2/9 liquids and other filling factors, the derivative measurements show the changes between the liquid and solid phases.

B. Conductivity measurements

This paragraph will discuss the subject of the systematic results of the conductivity measurements: the three-dimensional (3D) plot in Fig. 2(a) exhibits σ_{xx} for high $B \sim 19$–45 T, with an E-field range of 4.6–690 mV/cm. For convenience, the red guidelines highlight the data points for various filling factors: $\nu = 1/3$, 2/7, 1/4, 2/9, and 1/5. The data indicate the weakened solid phase and the sliding motion around the state of $\nu = 1/5$ (38 T), from which one can interpret that the FQHE liquid mixes with the lattice order. For a weak applied field ($E_{ac} = 4.6$ mV/cm), the zero conductivity can be interpreted as the localization of electrons at the WC lattice points. In the 3D plot, the onset of the solid phase is close to $B \sim 31$ T, which is close to the filling factor $\nu = 1/4$. The magnetoconductivity σ_{xx}, under the minimum $E_{ac} = 23$ mV/cm, exhibits a spike at $\nu \sim 1/5$ along the E

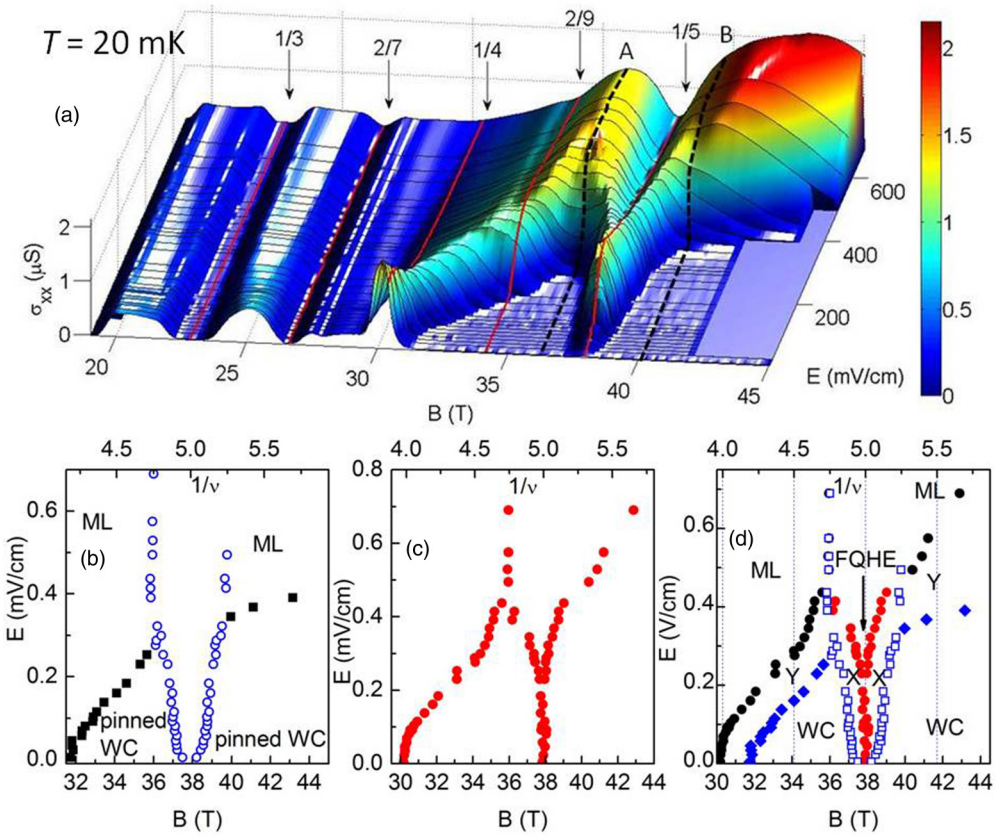

FIG. 2. (Color online) E-dependent conductivity measurement results. (a) The 3D plot for the longitudinal conductivity σ_{xx} under high B: 18–45 T, with $E \sim$ 0–690 mV/cm. The red traces highlight the filling factors. Also we highlight the divided ranges by the dotted lines, "A" and "B"; between those the robust $\nu = 1/5$ FQHE liquid shows a strong effect. (b) The black solid square curves are the boundary for totally pinned WC, and blue open circles indicate the robust influence by the $\nu = 1/5$ FQHE state. (c) The peak positions for the conductivity in panel (a), which can be clearly seen as the "mountain chain" in the 3D plot. (d) The phase diagram comes from the superposition of (b) and (c). In (b)–(d), the data are all shown under B and $1/\nu$.

axis, where the Wigner lattice order is rather weak. As the ac field increases, the immovable WC starts sliding, with the measured conductivity increasing sharply. Under an E field of 276 mV/cm, at $\nu = 1/5$, σ_{xx} reaches a peak value of 1.4 μS. When the applied dc field increases further, the conductivity starts to decrease dramatically, which is consistent with the result of the heating effect of the current. The σ_{xx} of the 1/5 state exhibits increases linearly in the small electric field of $E < 170$ mV/cm and decreases smoothly under large fields (200–690 mV/cm). Simultaneously, the nearby WC display distinct thresholds for $\nu > 1/5$ and $\nu < 1/5$. If we view the plot along the highlighted red curves (parallel to the E axis), the analysis of σ_{xx} is rather consistent with that of derivative measurements (dI/dV). When B is between 32 and 36 T or is higher than 40 T, overall, σ_{xx} increases almost linearly with the electric fields, which indicate that the WC starts to depin. On the other hand, for the remaining part (36–40 T) in the 3D plot, the influence of the 1/5 FQHE state is outlined by lines A and B. Line A highlights the extremal points of the conductivity between $\nu = 2/9 and 1/5$, and line B shows the transitional points of the phases for $\nu < 1/5$. These form the boundaries of the "V"-shape trough at high E regime. If the 1/5 state and the "V"-shaped valley section did not exist, the "mountain chain" of the WC phase would be continuous. In the similar case of the 2/9 state, the influence of FQHE liquid is much weaker than that of the 1/5 state. If we extract the characteristic data points from the 3D plot, panels (b) and (c) can be obtained consequently. In Fig. 2(b), the blue open circles show the boundary of the 1/5 influence, and the black solid squares outline the pinned WC area of the pure solid phase. The blue open circles come from the zero conductivities between 36 and 40 T [in panel (a)] for the low E-field regime, and the data points in line A and B for high E fields. This panel indicates the broad effect of the 1/5 FQHE liquid, which divides the WC phases into two parts. By contrast, Fig. 2(c) shows the intensive effect of the robust FQHE liquid at 1/5 and the broad effect of the surrounding WC for low electric field range. In high E range, under $B \sim$36 T, the peak positions are aligned with a straight line between 0.45 and 0.7 V/cm. Based on the analysis on Figs. 2(b) and 2(c), we obtain a phase diagram with respect to the electric field E and magnetic field B [Fig. 2(d)]. In the high E regime, the system is dominated by a liquid phase, denoted as the melted liquid (ML). The area of the "pure" WC is surrounded by the blue solid diamond and blue open square data points. In the intermediate E area, there exist two phases [panel (d)]: the "Y" phase and the "X" phase. The "Y" phase is a transition state, in which the WC and melted liquid mix, which has a rather distinct boundary. While the "X" phase can be quite different, the 1/5 FQHE liquid exerts an intensive influence in a wide vicinity, which is present within the range

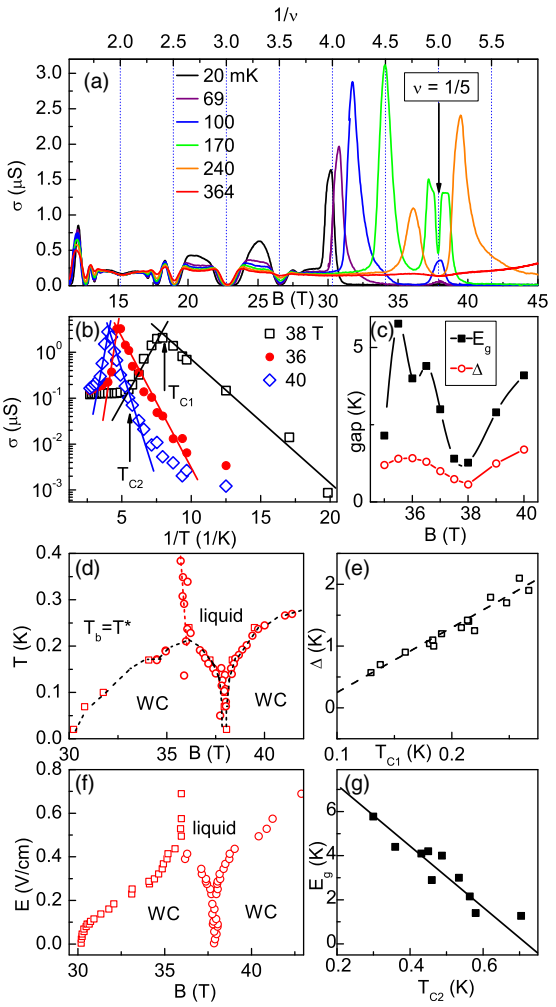

FIG. 3. (Color online) T-dependent conductivity results. (a) σ_{xx} under a T range of 20–370 mK; the top axis shows $1/\nu$. (b) The Arrhenius plot (σ_{xx} vs $1/T$) for 36, 38, and 40 T. (c) Energy gaps E_g and Δ under B fields: 34–40 T. The data follow $\sigma_{xx} \propto \exp(E_g/k_BT)$, $\sigma_{xx} \propto \exp(-\Delta/k_BT)$. (d) The boundary between the melted liquid and WC. The boundary T_b comes from the peak position in the T-dependent σ_{xx}, and T_{C1} is the transition temperature in the Λ-shape feature for fixed ν (B). (e) Δ vs T_{C1} presents a linear relation: $\Delta = 10.5T_{C1} - 0.8$ K. (f) Our obtained $E - T$ phase diagram is rather similar to the $E - B$ diagram. (g) In the E_g vs T_{C2} panel, the gap decreases with the critical T, with a gradient of -10.5.

of the red solid circle and the blue open square data. Finally, for the highest range of the E field, the FQHE liquid transitions into melted liquid. The blue open square data points separate "X" and "Y" phases.

In order to clarify the novel liquid-solid phase transition, we perform the T-dependent σ_{xx} experiments. Figure 3(a) displays zero conductivities for both liquid and solid phases, which are separated by a sharp peak. We observe FQHE states at $\nu = 1/3$ and 2/7, etc. For fixed temperatures, the σ_{xx} traces (versus sweeping B) show the transition between the FQHE liquid and WC (at $1/5 < \nu < 2/7$ and $\nu < 1/5$), and the peak intensities between the phases show the "contrast" between the phases. Here we describe the panel (a) data for varying temperature in detail.

(i) At base T of 20 mK, the conductivity in the vicinity of $\nu = 1/5$ is close to zero. Below 170 mK, as T increases, the σ_{xx} at $\nu = 1/5$ increases. The trace at 170 mK (green color trace) shows a significant minimum between two high nearby peaks (37.5 and 39 T). The σ_{xx} peak at 37.5 T shows the phase transition from the WC into the FQHE liquid. Similarly, the peak at 39 T displays the transition from FQHE liquid into WC. Qualitatively, the trace (170 mK) at the $\nu = 1/5$ state indicates an FQHE, and the nonzero minimum around 36 T exhibits a weak WC. Therefore as shown by the green color curve [in Fig. 3(a)], the electrons experience the liquid → solid → liquid → solid phases from low to high B fields. Combining all the traces for $T < 170$ mK, a competition between the WC and the FQHE liquid exists. The conductivity peaks between 30 and 35 T show the phase transition from the liquid phase into the solid phase. As the temperature goes up, both the B coordinate and the σ_{xx} peak intensity increase.

(ii) Above 170 mK, the conductivity at around the 1/5 filling factor starts to decrease, and the measured values for $\nu = 1/5$ at 240 and 364 mK are almost the same. The conductivity saturation indicates the FQH state at $\nu = 1/5$ for the high temperatures. The WC phase ($\sim$ 36 T) is rather faint while the liquid phases occur on both lower and higher magnetic fields. Therefore, the double peaks around 36 T merge and finally disappear. When temperature increases, the σ_{xx} at $\nu = 1/5$ increases to a maximum (0.55 μS) and then decreases. Based on the T-dependent conductivity, we qualitatively plot a dramatic phase diagram of solid and liquid in the B and T coordinates.

Moreover, in our quantitative analysis on the varying-T procedure, excitation energies in electron liquid and solid phases can be evaluated. The results in Fig. 3(b) are obtained by extracting the T-dependent data points for $B = 36$, 38, and 40 T. The result is that the T dependence of the conductivities has a sharp declining trend after a dramatic initial ascent. This type of "Λ"-shape traces is universal for the range of 35–42 T. In this panel, the Arrhenius plots show that the σ_{xx} is proportional to $\exp(E_g/k_BT)$, where E_g is presented as an energy scale independent of temperature. This energy scale can be viewed as the energy required by the transition from the ground state to the excited state. The other energy gap Δ for the WC area can be easily understood by using the Arrhenius equation: $\sigma_{xx} \propto (\exp - \Delta/k_BT)$. Compared with the neighboring WC ($B = 36$ and 40 T), both E_g ($\sim$1.27 K) and Δ ($\sim$0.57 K) of the $\nu = 1/5$ state are much lower [panel (c)]. The schematic of the phase diagram can also be displayed as in Fig. 3(d): the conductivity peak positions outline the phase boundary of the diagram in $B - T$ coordinates. For $B \sim$ 34–42 T, the data points enclose the solid phase in the low T range, with the liquid phase at higher temperatures. Above 450 mK and around 36 T, there is a straight line, along which the liquid phases on both sides merge, with a tiny conductivity peak in observations. Consequently, panel (e) presents a relation between the energy Δ and the critical point T_C: $\Delta = 10.5T_C$–0.8 K. The linear relation between the energy scales and the critical temperatures is universal. It is well known that in a BCS superconductivity with a weak electron correlation, the BCS gap is proportional to its T_C with a coefficient of 3.5 [29]. Similarly, panel (g) exhibits the linearlike behavior for E_g as in panel (e), which gives a negative gradient of -10.5.

Similarly in Fig. 3(d), the data points in Fig. 3(f) come from the peak positions of the "mountain chain" in E-dependent conductivity (Fig. 2). Consequently, we obtain the E-B and the T-B phase diagram. The trends of the σ_{xx} under varying E and T are strikingly similar [Figs. 3(d) and 3(f)]. The physics that underlines the phenomenon is as follows. The excited electric field drives the sliding motion of WC, and the heating leads to the solid melting. However, the concise E-T duality indicates an energy scale of 1 K which is equivalent to an E field of 2 V/cm. Consequently, a characteristic length of 450 nm is understood as the mean free path (l_0) in the solid phase in our 2D hole system. In fact, the strikingly simple duality between the E fields and the temperatures can be explained by the avalanche effect driven by the electric field [30]. In the impact ionization in semiconductors, the ionization rate (α) follows the relation $\alpha \sim \exp(-\varepsilon_i/k_BT) = \exp(-\varepsilon_i/eEl_0)$, which confirms our analysis of the results [in Figs. 3(d) and 3(f)]. Our experimental results show that the ionization rate α is proportional to the charge density and the conductivity. In a classical picture, the relation of $k_BT = eEl_0$ exists, where l_0 denotes the mean free path of the carriers. More importantly, in the weak pinning regime, the domain in the quantum solid keeps the phase coherent. The domain size is a long-sought problem in the research area of WC.

In our temperature-dependent experiments, the features on Δ versus T_{C1} and E_g versus T_{C2} in Figs. 3(e) and 3(g) are remarkable. The critical temperatures T_{C1} and T_{C2} are defined as the upper limits for phases. Similar cases exist in universal condensed-matter physics, i.e., superconductor-normal state transitions. Therefore, both of the energy-critical point relations are striking. We notice that the magnitudes for the positive and the negative gradients are both around 10.5. The dimensionless parameter may be relevant to the disorder pinning property. As shown in Fig. 3(b), the varying-T conductivities exhibit the "fluidity" of the liquid, which is manifested as the σ_{xx} feature. For instance, the fluidity at the base temperature is rather small due to the rare liquid order in the Wigner solid phase. At the turning point of the "Λ" feature, the fluidity drops dramatically. According to the E-T duality of $k_BT = eEl_0$, we also study the slopes of energies versus E fields in Figs. 3(e) and 3(g). The energy for panel (e) indicates the relation between the solid and liquid; it may be an energy gap or a "pinning gap." The "gap" and the slope lead to a characteristic length of 4.7 μm, which is around 10.5 times the value of l_0. The energy scale shown in panel (g) is used for describing the phase transition from the liquid-dominant mixing state to melted Fermi liquid. The solid-liquid mixing state may include sliding domain WC and melted liquid in our specimen.

As we discussed in the preceding text, some characteristic lengths are crucial for weak pinning WC. In our sample, the WC lattice constant of $a = 25$ nm is obtained from the relation of $\nu = (4\pi/\sqrt{3})(l_B/a)^2$ [19]. In the weak pinning case we consider the Larkin length R_C [17], which plays the role of the pinning length. Fogler and Huse interpreted that the R_C is both the mean free path in a classical model and the localization length of the quantum solid phase; the latter can be understood as the actual domain size for the weak pinning WC [16]. Compared to the microwave measurements for WC pinning modes in low density 2DES [19], our result on the domain size for 2DHS is three times the size of theirs (~100–200 nm), and $R_C \sim 18a$ is not far from that in their report.

C. Phase diagram

We have explained some details of the systematic phase diagram in Fig. 2(d). The zero conductivity indicates that the pure phase of WC was totally pinned in Fig. 2(a). On the other hand, the thresholds [Figs. 1(a) and 1(b)] display the boundary for depinning the Wigner solid. Consequently they show a consistent outline in the same way as the "pure" WC (blue solid square data points) in Fig. 2(b). More strikingly, the unusual features (34 and 39 T) in Fig. 1(a) can also be explained within our phase diagram. $\nu = 2/9$ exists at $B \sim 34$ T, which is a special regime in the phase diagram. In this regime, we observe two distinct slopes in the derivative measurements: before the WC solid transitions into the melted liquid, it has to go through a weak FQHE liquid. Simultaneously, at 39 T the state experiences WC $\rightarrow$ vicinity of 1/5 FQHE liquid $\rightarrow$ melted liquid (three phases) in our dI/dV measurements. Figure 4(a) shows the conductivity data points in the frame of E (or T) versus magnetic field B, with $1/\nu$ present in the top axis. The phase diagram [Fig. 4(a)] is an important result, which comes from the competition between the CF liquid ($\nu = 2/9$ and 1/5) and WC. In our "Λ" feature in the T-dependent results, the competition between the WC and 1/5 FQHE is distinctive. The WC dominate the base temperature, while the state varies according to the temperature. In higher T range, 1/5 liquid overwhelms the WC phase. Compared to the 2/9 state, the 1/5 liquid is much stronger, with surrounding ν (or magnetic fields) occupied by composite Fermion liquid. The 1/5 state (and 2/9 state) area in the phase diagram is consistent with those summarized from Figs. 2, 3(d), and 3(f), respectively. The 1/5 state appears around the base T and develops completely at intermediate temperatures, while the sign of the 2/9 state only appears at intermediate T. If we read the results in another way, along the T coordinate, the Wigner solid phase has a lower ground state than both the 2/9 and 1/5 FQHE states at base temperature. In an ideal case, the WC solid would occupy the base temperature and the 1/5 state would dominate in a very narrow regime at finite temperatures.

In our observation, the unusual RIP around $\nu = 1/5$ is first discovered in the 2DHS. Based on the previous reports, the RIP is observed around $\nu = 1/3$ in 2DHS [9], and around 1/5 in 2DES [4]. In our 2D hole sample, r_s reaches a maximum of ~7.6 owing to the very high carrier density (p). A plausible explanation in our experiments is that the short-range interaction and the narrow (20-nm) quantum-well structure help to form the liquid state at $\nu = 1/5$ [31]. Generally, the reentrant quantum Hall liquid only appears when QW width (W) is more than about five times the magnetic length [31]. The ratio $W/l_B \sim 5$ reaches the critical value for the liquid state form at $\nu = 1/5$ in our observations.

Based on our phase diagram, the "X" phase area (around $\nu = 1/5$) indicates the coexistence of composite fermion liquid ($\nu = \frac{n}{2pn+1}$ with $n = 1$ and $p = 2$) and WC in the low-temperature regime. Although the WC dominate near base temperature, the boundary temperature T_B for $\nu = 1/5$ is relatively low. The details in the phase diagram in Fig. 4(a)

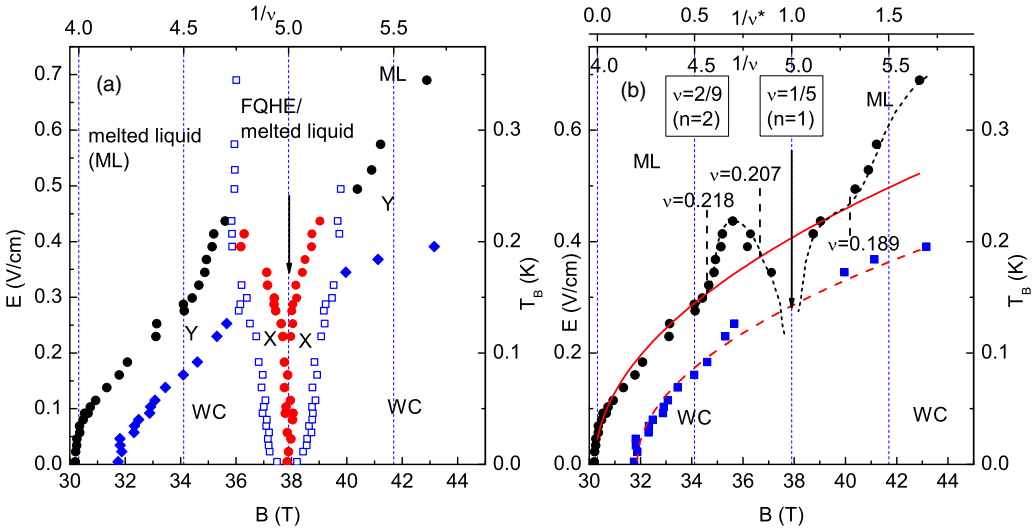

FIG. 4. (Color online) The phase diagram under $B - T_B$ (boundary temperature) or $B - E$ coordinates. (a) This panel combines the data from Fig. 3(d) and the $E - T$ duality, with the E axis (left axis) and T_B axis (right axis) in it. (b) The data fittings are carried out for the phase boundaries. The red fitting curves for the black circle and the blue square data follow the relations $T_B \propto (B - B_0)^{1/2}$. In the range of $1/5 < \nu < 2/9$ and $\nu < 1/5$, there are dramatic protuberances (outlined by the black short dashed line). The inverse of filling factor ν and the CF fillings ν^* axis are shown too.

show the CF-WC ("X"-phase) coexisting around $\nu = 1/5$. As in the regular CF theory, rational filling of $\nu = \frac{n}{2pn+1}$ can be mapped to integer nth Λ filling level of CF.

In the presence of a weak disorder, at CF fillings close to $\nu^* = n$, the CF crystal and CF liquid coexistence forms the type-2 CFWC, which is different from the type-1 CF crystal at very low fillings [21]. A small density of composite fermions or CF holes at the nearby fillings around the ($\nu^* = n$) integer ΛLs helps the formation of the type-2 CFWC [21]. Their conclusions match very well with the microwave resonance measurements at $\nu = 1/3$ in 2DES [23]: a WC pinning mode was observed in a narrow fillings range around $\nu = 1/3 \pm 0.015$, while the other pinning mode locates in a much wider regime. More recently, a theoretical report proposed the existence of a solid state between $\nu = 1/5$ and 2/9 FQHE states, where the phases interplay between type-1 and type-2 CF crystals [22]. Around $\nu = 1/5$ and 2/9 the type-2 CF crystal has a lower ground-state energy, and the type-1 CF crystal has lower energy between the two fillings [32].

The phase boundaries for the insulating phase and liquid are shown in Figs. 4(a) and 4(b). The onset for the IP is close to $\nu = 1/4$ ($B \sim 30$ T), at which the effective magnetic field $B^* \sim 0$ for ^{4}CF. The phase boundary for the solid and melted liquid is shown with the black circle data points, and the blue square data separate the pinned and sliding WC phases. Both boundaries can be fitted as the square-root function: $T_B \propto (B - B_0)^{1/2}$ [Fig. 4(b)], which is qualitatively similar to the $T - B$ phase diagram [22]. Simultaneously, the transition area between $\nu = 1/5$ ($n = 1$) and 2/9 ($n = 2$) shows the clear deviation of phase boundary from the fitting curves (red solid line). In the $\nu \lesssim 2/9$ and $\nu < 1/5$ regime, the boundary temperatures increase sharply with B, forming protuberances (black short-dashed line) above the fitting curve. Therefore the solid-liquid boundary can be visibly understood as the protuberances superposed on the square-root function curve. The protuberances appear at the range of $\nu \sim (0.207–0.218)$ and $\nu < 0.189$ [32]. Below $T_B \sim 0.15$ K, FQHE liquid exists in a very narrow area around $\nu \sim 1/5$ [Fig. 4(a)]. In the nearby regime of $\nu < 0.1996$ ($\nu^* = 1 - 0.010$) and $\nu > 0.2010$ ($\nu^* = 1 + 0.025$), the Wigner crystal dominates below 0.1 K. The coexistence of CF-WC at $\nu \sim 1/5$ and the solids nearby filling around $\nu^* \sim (n = 1)$ may lead to the novel type-2 CFWC [32]. The phase boundary (black circle data) shows that the ground-state energy for the $\nu = 1/5$ liquid is close to the WC. However, the WC has a lower ground-state energy than that of the liquid at $\nu = 2/9$. Although our data analysis seems to indicate the existence of the CFWC, we must note that we cannot totally rule out an explanation of the electron Wigner crystals around $\nu \sim 1/5$ in 2DHS.

III. CONCLUSIONS

In summary, a schematic phase diagram is described as the following: for $B \sim$ 34–38 and 38–42 T, the universal IP-liquid transition exists under low T. WC dominates at base temperature in a wide range of filling factors, and FQHE states of 2/9 and 1/5 (in ^{4}CF regime) both appear at intermediate T. Therefore competition exists between the IP and FQHE liquid and there is a very sharp contrast. Around $\nu \sim 1/5$, the robust FQHE liquid competes (or coexists) drastically with the WC solid. On the other hand, the weakly pinned WC displays an unexpected E-T duality, which may be caused by the avalanche effect driven by an electric field. More importantly, we evaluate the characteristic length of 450 nm, which can be the domain size of the weakly pinned WC. In further analysis on $\nu \sim 1/5$, there may be some indications of the novel CF crystal in the four flux composite fermion regime.

ACKNOWLEDGMENTS

We grateful acknowledge Changli Yang, Yuan Li, Lu Yu, and Junren Shi for useful discussions. The work

at Rice is supported by U.S. Department of Energy Grant No. DE-FG02-06ER46274 (measurement) and by NSF Grant No. DMR-1207562 (sample preparation); C.Z. was supported by a Keck Foundation. C.Z. performed experiments; C.Z. and R.R.D analyzed data and wrote the paper; L.P., M.M., and K.W. grew the semiconductor wafers; R.R.D conceived and supervised the project.

[1] E. Wigner, Phys. Rev. **46**, 1002 (1934).
[2] D. C. Tsui, H. L. Stormer, and A. C. Gossard, Phys. Rev. Lett. **48**, 1559 (1982).
[3] Y. P. Li, Ph.D. thesis, Princeton University, 1994.
[4] T. Sajoto, Y. P. Li, L. W. Engel, D. C. Tsui, and M. Shayegan, Phys. Rev. Lett. **70**, 2321 (1993).
[5] M. B. Santos, J. Jo, Y. W. Suen, L. W. Engel, and M. Shayegan, Phys. Rev. B **46**, 13639(R) (1992).
[6] T. Sajoto, Ph.D. thesis, Princeton University, 1993.
[7] Y. P. Li, T. Sajoto, L. W. Engel, D. C. Tsui, and M. Shayegan, Phys. Rev. Lett. **67**, 1630 (1991).
[8] V. J. Goldman, M. Santos, M. Shayegan, and J. E. Cunningham, Phys. Rev. Lett. **65**, 2189 (1990).
[9] M. B. Santos, Y. W. Suen, M. Shayegan, Y. P. Li, L. W. Engel, and D. C. Tsui, Phys. Rev. Lett. **68**, 1188 (1992).
[10] G. A. Csathy, H. Noh, D. C. Tsui, L. N. Pfeiffer, and K. W. West, Phys. Rev. Lett. **94**, 226802 (2005).
[11] R. L. J. Qiu, X. P. A. Gao, L. N. Pfeiffer, and K. W. West, Phys. Rev. Lett. **108**, 106404 (2012).
[12] G. Grüner, Rev. Mod. Phys. **60**, 1129 (1988).
[13] H. Fukuyama, J. Phys. Soc. **41**, 513 (1976).
[14] H. Fukuyama and P. A. Lee, Phys. Rev. B **17**, 535 (1978); **18**, 6245 (1978).
[15] H. A. Fertig, Phys. Rev. B **59**, 2120 (1999).
[16] M. M. Fogler and D. A. Huse, Phys. Rev. B **62**, 7553 (2000).
[17] A. I. Larkin, Sov. Phys. JETP **31**, 784 (1970).
[18] A. I. Larkin and Y. N. Ovchinnikov, J. Low Temp. Phys. **34**, 409 (1979).
[19] P. D. Ye, L. W. Engel, D. C. Tsui, R. M. Lewis, L. N. Pfeiffer, and K. West, Phys. Rev. Lett. **89**, 176802 (2002).
[20] C.-C. Chang, G. S. Jeon, and J. K. Jain, Phys. Rev. Lett. **94**, 016809 (2005).
[21] A. C. Archer and J. K. Jain, Phys. Rev. B **84**, 115139 (2011).
[22] A. C. Archer, K. Park, and J. K. Jain, Phys. Rev. Lett. **111**, 146804 (2013).
[23] H. Zhu, Y. P. Chen, P. Jiang, L. W. Engel, D. C. Tsui, L. N. Pfeiffer, and K. W. West, Phys. Rev. Lett. **105**, 126803 (2010).
[24] Z. Q. Yuan, R. R. Du, M. J. Manfra, L. N. Pfeiffer, and K. W. West, Appl. Phys. Lett. **94**, 052102 (2009).
[25] H. A. Fertig and M. Shayegan, in *Perspectives in Quantum Hall Effects*, edited by S. Das Sarma and A. Pinczuk (Wiley, New York, 1997), Chaps. 5 and 9, respectively.
[26] Y. P. Chen, R. M. Lewis, L. W. Engel, D. C. Tsui, P. D. Ye, Z. H. Wang, L. N. Pfeiffer, and K. W. West, Phys. Rev. Lett. **93**, 206805 (2004).
[27] X. Zhu, P. B. Littlewood, and A. J. Millis, Phys. Rev. Lett. **72**, 2255 (1994).
[28] X. Zhu, P. B. Littlewood, and A. J. Millis, Phys. Rev. B **50**, 4600 (1994).
[29] D. J. Scalapino, *Superconductivity*, edited by by R. D. Parks (Dekker, New York, 1969), pp. 449–559.
[30] K. Seeger, *Semiconductor Physics: An Introduction*, 9th ed., (Springer, New York, 2004), Chap. 10.
[31] Y. Liu, D. Kamburov, S. Hasdemir, M. Shayegan, L. N. Pfeiffer, K. W. West, and K. W. Baldwin, Phys. Rev. Lett. **113**, 246803 (2014).
[32] See the phase diagram in Ref. [22]; at low temperature, for $\nu > 2/9$ there are no CF crystals. The filling factor range for the reentrant crystal is $0.207 < \nu < 0.218$, in which the type-1 CF crystal has lower energy than the type-2 CF crystal (the FIG. 3 in Supplemental Materials of Ref. [22]). Around $\nu \sim 1/5$, the type-2 CF crystal may have lower energy than that of the type-1 CF crystal. Below $\nu \sim 0.18$, the phase may indicate a transition into the ^{4}CF crystal.